Chinese Physics B

PAPER

Ion-specific hydration structures revealed by SCAN-based *ab initio* simulations

To cite this article: Tiancheng Liang *et al* 2025 *Chinese Phys. B* **34** 126102

Chin. Phys. B **34**, 126102 (2025)

Ion-specific hydration structures revealed by SCAN-based *ab initio* simulations

Tiancheng Liang(梁天成)[1,†], Liying Zhou(周丽颖)[1,2,†], Yizhi Song(宋易知)[1,3,†], Xifan Wu[3,4], and Limei Xu(徐莉梅)[1,5,6,‡]

[1] *International Center for Quantum Materials, School of Physics, Peking University, Beijing* 100871*, China*
[2] *Postdoctoral Research Station of China CITIC Bank, Beijing* 100026*, China*
[3] *Department of Physics, Temple University, Philadelphia, Pennsylvania* 19122*, United States*
[4] *Institute for Computational Molecular Science, Temple University, Philadelphia, Pennsylvania* 19122*, United States*
[5] *Interdisciplinary Institute of Light-Element Quantum Materials and Research Center for Light-Element Advanced Materials, Peking University, Beijing* 100871*, China*
[6] *Collaborative Innovation Center of Quantum Matter, Beijing* 100871*, China*

(Received 22 July 2025; revised manuscript received 28 September 2025; accepted manuscript online 14 October 2025)

Hydrated ions play essential roles in diverse chemical and biological processes, yet accurately characterizing their hydration structures remains challenging due to the delicate interplay of ion–water and water–water interactions. Here, we use *ab initio* molecular dynamics (AIMD) simulations based on the strongly constrained and appropriately normed (SCAN) exchange–correlation functional to systematically investigate the hydration structures of eight representative ions (Mg^{2+}, Ca^{2+}, Li^+, Na^+, K^+, F^-, Cl^-, Br^-) in aqueous solution. Compared to the widely used Perdew–Burke–Ernzerhof (PBE) functional, SCAN substantially improves the description of solvent water by weakening the hydrogen-bond network and enhancing structural disorder, yielding results in closer agreement with experiments. SCAN modifies ionic hydration shells in an ion-specific manner, governed by ionic size and charge, and reproduces experimental hydration geometries especially well for intermediate-size monovalent ions (Na^+, Cl^-). Moreover, SCAN consistently reduces the overpolarization of water molecules near ions. These improvements lead to more accurate and physically consistent hydration structures, highlighting SCAN's utility for modeling complex aqueous systems and offering guidance for future studies of ionic solvation.

Keywords: ion hydration, solvent structure, SCAN functional, *ab initio* molecular dynamics

PACS: 61.20.Qg, 31.15.eg, 02.70.Ns, 82.20.Wt

DOI: 10.1088/1674-1056/ae12d2 **CSTR:** 32038.14.CPB.ae12d2

1. Introduction

Hydrated ions are ubiquitous in nature and biology, playing critical roles in diverse physical and biochemical processes, such as seawater desalination,[1] atmospheric aerosols formation,[2] salt dissolution,[3] and ion transport through channels.[4,5] Understanding the atomic-level structures and properties of hydrated ions has thus remained a long-standing challenge,[6–10] requiring accurate description of both water–water and ion–water interactions. The hydrogen-bond (H-bond) network in liquid water emerges from a subtle interplay among intramolecular O–H covalent bonds, intermolecular H-bonds, and van der Waals (vdW) forces. The introduction of ions disrupts this network by introducing strong local electrostatic fields and thereby reshaping the structure and dynamics of the surrounding water molecules.

Experimental probes, such as scattering,[11–14] diffraction,[15–18] and vibrational spectroscopy,[19–22] have yielded valuable ensemble-averaged information about hydration shells. However, the limited spatial and temporal resolution of these techniques hinders direct access to transient or fluctuating local structures. Although ultrafast vibrational energy transfer measurement[23,24] and scanning probe methods[25–27] have shed light on hydration at the molecular level, capturing its full dynamics and microscopic complexity remains a significant experimental challenge.

Density functional theory (DFT) based-*ab initio* molecular dynamics (AIMD) simulations[28,29] offer a powerful alternative, enabling molecular-level insights into ionic hydration with temporal resolution beyond current experimental reach. Yet, the accuracy of AIMD critically depends on the exchange–correlation (XC) functional employed. Early AIMD simulations using generalized-gradient approximation (GGA) functionals, such as Perdew–Burke–Ernzerhof (PBE), predicted overly structured tetrahedral water networks.[30] The subsequent inclusion of vdW interactions, for example via the Tkatchenko–Scheffler (TS-vdW) correction, markedly softened the H-bond network, yielding liquid water and hydrated ion structures in better agreement with experiment.[31]

A recent development is the SCAN meta-GGA functional,[32] which satisfies all 17 known exact constraints for semilocal XC functionals. SCAN accurately describes a wide variety of bonding types — including covalent, ionic,

---

[†] These authors contributed equally to this work.

[‡] Corresponding author. E-mail: limei.xu@pku.edu.cn

metallic, hydrogen bonding, and vdW interactions[33] — and has been shown to reproduce the structure, energetic, and dynamics of liquid water with high fidelity.[34] SCAN's success arises from its accurate treatment of the delicate balance between covalent bonding, intermolecular hydrogen bonding and dispersion forces, without requiring empirical vdW corrections.

In this work, we employ AIMD simulations with the SCAN functional to investigate the hydration structures of eight representative ions (Mg^{2+}, Ca^{2+}, Li^{+}, Na^{+}, K^{+}, F^{-}, Cl^{-}, Br^{-}) in aqueous solutions. We show that SCAN produces universal modifications to solvent water structure, weakening the H-bond and enhancing structural disorder. At the same time, SCAN exhibits ion-specific effects that depend on ion size and charge, as these parameters control the strength of ion–water electrostatic interactions. For isocharged ions, the hydration shell becomes increasingly diffuse with large ionic radii, and SCAN further accentuates this trend by reducing overpolarization of water molecules. For the systems examined, SCAN generally produces results in better agreement with experimental observations. These findings demonstrate the practical utility of SCAN in modeling ionic aqueous systems and highlight its advantages over conventional functionals in capturing both universal and ion-dependent hydration phenomena.

2. Computational methods

Born–Oppenheimer molecular dynamics (BOMD) simulations were performed within canonical (NVT) ensemble using a modified version of the Quantum ESPRESSO code package.[35,36] Each of the eight ionic aqueous systems — Mg^{2+}, Ca^{2+}, Li^{+}, Na^{+}, K^{+}, F^{-}, Cl^{-}, Br^{-} — was modeled in a periodic cubic cell (12.44 Å side length) containing one ion and 63 water molecules at 363 K, following the simulation protocol of Ref. [31], with the same cell size and composition of the system adopted in Refs. [37–39]. It is worth noting that Ref. [38] reported that ion–oxygen radial distribution functions are not sensitive to system size and that a system with 63 water molecules is already sufficient to describe the first and second solvation shells. For comparison, simulations for bulk water were also conducted using 64 water molecules in the same cell.

Electronic exchange and correlation were treated using the SCAN meta-GGA functional, with the pure PBE functional used for benchmarking. This ensures that the comparison reflects only the intrinsic differences between the two functionals. Core–electron interactions were described using norm-conserving pseudopotentials: the Hamann–Schlüter–Chiang–Vanderbilt construction[40,41] was used for H, O and K, and the optimized-norm conserving Vanderbilt construction[42,43] was employed for Mg, Ca, Li, Na, F, Cl and Br. A kinetic energy cutoff of 85 Ry was used for plane-wave expansions, and the Brillouin zone was sampled at the Γ point.

All simulations were equilibrated for more than 30 ps, with temperature controlled via Nosé–Hoover chain thermostats.[44,45] To suppress quantum nuclear effects and enable a larger integration time step, hydrogen atoms were replaced by deuterium;[46,47] this approximation is known not to affect static structural properties when ions are treated classically. The equations of motion were integrated using the velocity Verlet algorithm with a 0.48 fs time step. At each time step, electronic ground states were converged via damped dynamics,[48] with a total energy convergence threshold of 0.5×10^{-7} Hartree.

3. Results and discussion

3.1. Structures of solvent water

The semilocal PBE functional is widely used in simulations of aqueous systems, yet it is well established that PBE overestimates H-bond strength and network rigidity,[30] leading to underestimated diffusivity at ambient conditions when compared with scattering and diffraction experiments. To mitigate this, simulations using PBE often require elevated temperatures (e.g., 360–400 K) to match room-temperature behavior.[49–51] To better characterize the H-bond network in ionic aqueous environments, we compare the performance of SCAN with that of PBE across eight ionic solutions.

Table 1. Tabulated summary of the structural properties of ionic aqueous solutions considered in this work obtained by PBE and SCAN functionals. From left to right, the positions (in Å) and intensities of the first maximum ($r^{\max1}$ and $g_{\mathrm{O-O}}^{\max1}$); the first minimum ($r^{\min1}$ and $g_{\mathrm{O-O}}^{\min1}$) of the corresponding $g_{\mathrm{O-O}}(r)$; the average number of H-bonds n_{HB} per water molecule. The available experimental data are provided in the last row.

System	Functional	$r^{\max1}$	$g_{\mathrm{O-O}}^{\max1}$	$r^{\min1}$	$g_{\mathrm{O-O}}^{\min1}$	n_{HB}
Mg^{2+}	PBE	2.73	2.77	3.39	0.57	3.58
	SCAN	2.75	2.57	3.52	0.81	3.36
Ca^{2+}	PBE	2.73	2.92	3.31	0.59	3.65
	SCAN	2.75	2.54	3.55	0.86	3.36
Li^{+}	PBE	2.73	3.04	3.31	0.56	3.70
	SCAN	2.78	2.55	3.56	0.87	3.39
Na^{+}	PBE	2.73	2.88	3.28	0.55	3.66
	SCAN	2.75	2.52	3.55	0.87	3.39
K^{+}	PBE	2.70	3.00	3.29	0.49	3.72
	SCAN	2.78	2.53	3.52	0.87	3.42
F^{-}	PBE	2.70	2.71	3.28	0.51	3.56
	SCAN	2.75	2.37	3.47	0.85	3.31
Cl^{-}	PBE	2.71	2.71	3.25	0.49	3.59
	SCAN	2.75	2.34	3.55	0.82	3.31
Br^{-}	PBE	2.73	2.75	3.25	0.52	3.59
	SCAN	2.75	2.20	3.55	0.81	3.27
Pure water	Expt.[52]	2.76	2.62	3.42	0.82	–

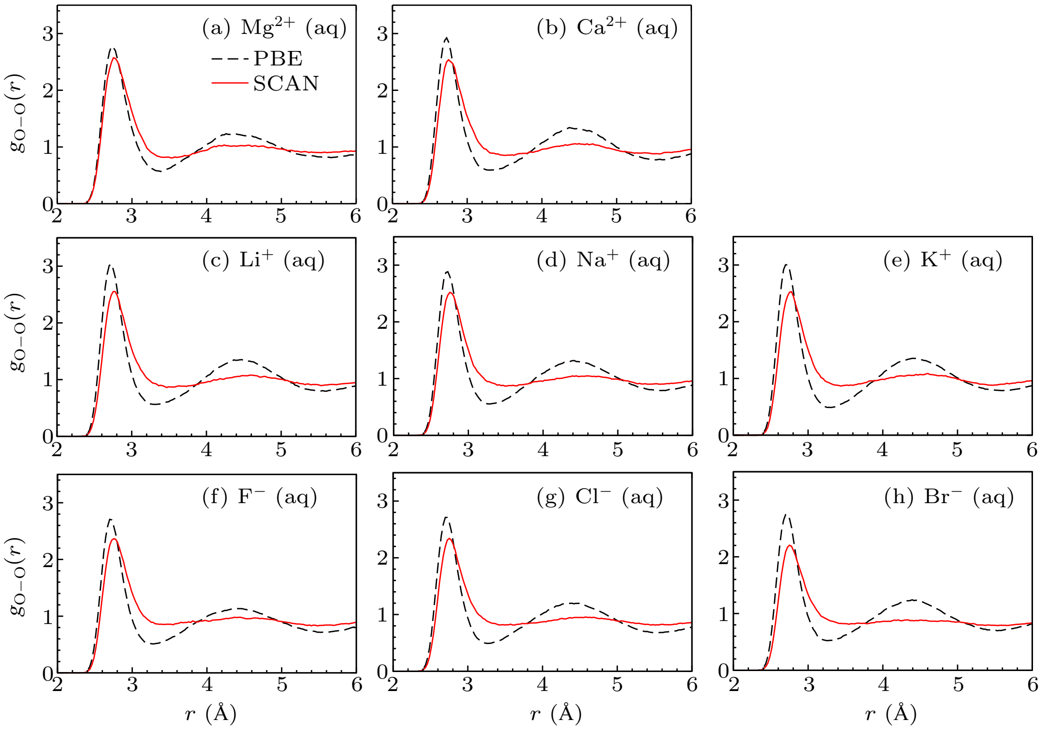

Fig. 1. Oxygen–oxygen radial distribution functions (RDFs) in ionic aqueous solutions. RDFs $g_{\mathrm{O-O}}(r)$ were computed for (a) Mg^{2+}, (b) Ca^{2+}, (c) Li^{+}, (d) Na^{+}, (e) K^{+}, (f) F^{-}, (g) Cl^{-}, (h) Br^{-} aqueous solutions using the PBE and SCAN functionals. These curves reflect the structural organization of solvent water in the presence of different ions.

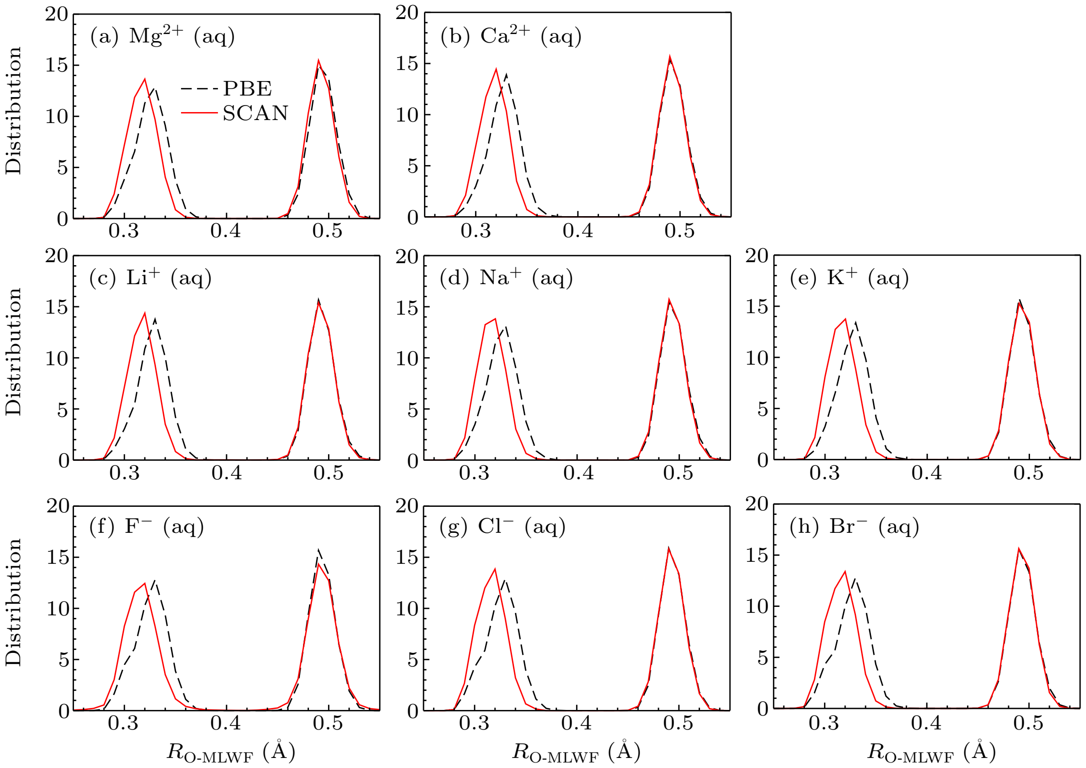

Fig. 2. Distributions of O-MLWF center distance in ionic aqueous solutions. The distances between oxygen atoms and the centers of maximally localized Wannier functions (MLWFs) were computed for (a) Mg^{2+}, (b) Ca^{2+}, (c) Li^{+}, (d) Na^{+}, (e) K^{+}, (f) F^{-}, (g) Cl^{-}, (h) Br^{-} aqueous solutions using the PBE and SCAN functionals. These distributions reflect changes in electronic polarization and lone-pair localization of water molecules induced by different ions and the choice of exchange–correlation functional.

Even at 363 K, PBE yields an over-structured water network, as revealed by the oxygen–oxygen radial distribution function (RDF) $g_{\mathrm{O-O}}(r)$ (Fig. 1, Table 1). In contrast, SCAN substantially softens the liquid structure, providing much closer agreement with experimental data.[52] This improvement stems from SCAN's treatment of intermediate-range vdW interactions, which introduce non-directional attractions among water molecules. Consequently, SCAN shifts the first coordination-shell peak outward — from $r^{\max1} = 2.70$–2.73 Å (PBE) to 2.75–2.78 Å (SCAN) — and enhances population in the interstitial region, as shown by an increase in the first minimum $g_{\mathrm{O-O}}^{\min1}$ from 0.49–0.59 to 0.81–0.87 (Table 1). These features collectively point to a less rigid, more disordered solvent network under SCAN.

To elucidate the microscopic origin of this structural softening, we examine the covalent O–H bond via the oxygen-hydrogen RDF $g_{\mathrm{O-H}}(r)$. The first peak position, $r^{\max1}$, corresponds to the most probable covalent bond length, while the peak height $g_{\mathrm{O-H}}^{\max1}$ serves as a proxy for bond strength. Under SCAN, $g_{\mathrm{O-H}}^{\max1}$ increases from 32.59–32.98 to 35.96–36.61 and the bond length shortens from 0.990 Å to 0.974 Å (Table 2), suggesting stronger covalent character, which suppresses proton delocalization and thus reduces H-bond donation.

Table 2. The positions (in Å) and intensities of the first maximum ($r^{\max1}$ and $g_{\mathrm{O-H}}^{\max1}$) of the corresponding $g_{\mathrm{O-H}}(r)$ considered in this work obtained by PBE and SCAN functionals.

	Functional	Mg^{2+}	Ca^{2+}	Li^+	Na^+	K^+	F^-	Cl^-	Br^-
$r^{\max1}$	PBE	0.990	0.990	0.990	0.990	0.990	0.990	0.990	0.990
	SCAN	0.974	0.974	0.974	0.974	0.974	0.974	0.974	0.974
$g_{\mathrm{O-H}}^{\max1}$	PBE	32.98	32.62	32.72	32.66	32.73	32.69	32.82	32.59
	SCAN	36.26	36.36	36.37	36.27	36.61	35.96	36.21	36.18

This picture is further corroborated by electronic structure analysis using maximally localized Wannier functions (MLWFs).[53,54] As shown in Fig. 2, the distribution of MLWFs centers for water molecules reveals two peaks associated with lone pairs and bonding electron pairs. Under SCAN, the lone-pair centers shift closer to the O nucleus, while the bonding pairs remain largely unchanged. The inward contraction of lone pairs diminishes electrostatic interactions with neighboring protons, thereby weakening H-bond formation.

The extent of hydrogen bonding in all eight ionic aqueous solutions is quantified by the average number of H-bonds per water molecule, n_{HB}, using the geometric criterion introduced by Luzar and Chandler.[55] As summarized in Table 1, SCAN consistently reduces n_{HB} across all systems — from 3.56–3.72 under PBE to 3.27–3.42 under SCAN — indicating a clearly reduced H-bond connectivity. Further insights are provided by the distribution of hydrogen-bonding topologies (Fig. 3). The population of A_2D_2-type configurations — where water molecules simultaneously donate and accept two H-bonds, indicative of tetrahedral coordination — drops from $\sim 60\%$ under PBE to $\sim 40\%$ under SCAN. This loss is compensated by an increase in A_1D_1, A_1D_2 and A_2D_1 configurations, which reflect partially broken H-bond environments.

Figures 1–3 present quantities such as O–O RDFs, O–H bond lengths, and hydrogen-bond donor/acceptor distributions. These provide theoretical insights into single-ion effects on water structure. Direct experimental analogues for such isolated-ion systems are not available. Notably, the solvent water behaves similarly across different ions under both

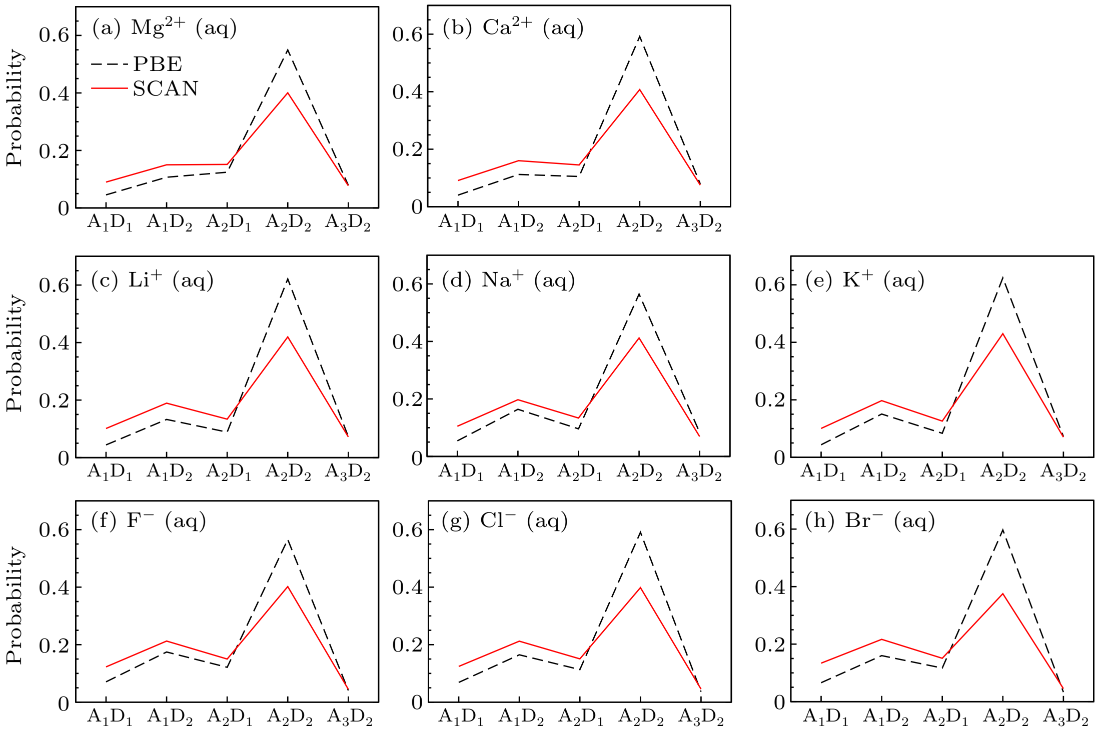

Fig. 3. Probability distributions of H-bond configurations in ionic aqueous solutions. Probability distributions of hydrogen-bond configurations were obtained for aqueous solutions of (a) Mg^{2+}, (b) Ca^{2+}, (c) Li^+, (d) Na^+, (e) K^+, (f) F^-, (g) Cl^-, (h) Br^- using the PBE and SCAN simulations. Each configuration is labeled as A_xD_y, where x and y denote the numbers of accepted (A_x) and donated (D_y) H-bonds per water molecule, respectively. Here, we only show these five types, as the distributions of other types are much smaller and have been omitted for clarity.

XC functionals, in agreement with previous spectroscopic and simulation studies,[56] suggesting that ion effects on the H-bond network are largely confined within the hydration shell. Meanwhile, these observations confirm that SCAN systematically disrupts the ideal tetrahedral H-bond framework, yielding a more structurally disordered liquid environment that is consistent with experiments.

3.2. Hydration structures of ions

Building on the reduced H-bond connectivity in the solvent, we now examine how SCAN influences the hydration structure of individual ions. The degree of structural modification exhibits strong ions specificity, as shown in Figs. 4–6 and Table 3. For clarity, we group the ions into three categories—divalent cations (Mg^{2+} and Ca^{2+}), monovalent cations (Li^+, Na^+, K^+), and monovalent anions (F^-, Cl^-, Br^-). Ion–oxygen RDFs, $g_{\text{ION–O}}(r)$, are used to characterize the ion hydration environment. Coordination numbers (CNs) are computed by integrating the RDFs up to their first minima $r^{\min1}$. In addition, we extract CN probability distribution and O-ion-O angular distributions from the AIMD trajectories to capture both the statistical variation and angular ordering within the hydration shell. These analyses reveal that SCAN alters the hydration shell structure in an ion-specific fashion. Ions with larger radii or lower charge densities exhibit more diffuse hydration shells under SCAN, consistent with weaker ion–water electrostatic interactions and a solvent environment with reduced H-bond rigidity.

Table 3. Tabulated summary of the structural properties of ionic aqueous solutions considered in this work obtained by PBE and SCAN functionals. From left to right, the positions (in Å) and intensities of the first maximum ($r^{\max1}$ and $g^{\max1}_{\text{ION–O}}$), the first minimum ($r^{\min1}$ and $g^{\min1}_{\text{ION–O}}$), and the second maximum ($r^{\max2}$ and $g^{\max2}_{\text{ION–O}}$) of the corresponding $g_{\text{O–O}}(r)$; the average CN of the eight ions and the distribution of CN. The available experimental data are provided for comparison.

System	Ionic radius	Functional	$r^{\max1}$	$g^{\max1}_{\text{ION–O}}$	$r^{\min1}$	$g^{\min1}_{\text{ION–O}}$	$r^{\max2}$	$g^{\max2}_{\text{ION–O}}$	CN	Distribution of CN
Mg^{2+}	0.72 Å	PBE	2.09	13.61	3.01	0.00	4.26	2.33	6.00	6
		SCAN	2.06	14.81	3.02	0.00	4.21	2.06	6.00	6
		Expt.[58]	2.09	–	–	–	–	–	6.00	–
Ca^{2+}	0.99 Å	PBE	2.37	9.59	3.16	0.00	4.42	2.07	6.00	6
		SCAN	2.41	9.71	3.12	0.06	4.55	1.88	7.16	6–8
		Expt.[15]	2.42	–	–	–	–	–	6.00	–
Li^+	0.76 Å	PBE	1.96	8.78	2.78	0.006	4.07	1.58	4.00	4
		SCAN	1.93	8.88	2.78	0.06	4.05	1.63	4.09	3–5
		Expt.[62]	1.96	–	–	–	–	–	3.90	–
Na^+	1.02 Å	PBE	2.35	5.15	3.12	0.21	4.34	1.46	4.81	4–6
		SCAN	2.35	5.19	3.18	0.35	4.39	1.30	5.43	4–7
		Expt.[19]	2.37	–	–	–	–	–	5.40	–
K^+	1.38 Å	PBE	2.70	3.40	3.55	0.61	4.60	1.32	6.00	4–8
		SCAN	2.75	3.47	3.65	0.57	4.82	1.20	7.29	5–10
		Expt.[63]	2.73	–	–	–	–	–	6.10	–
F^-	1.33 Å	PBE	2.57	4.28	3.18	0.22	4.37	1.57	4.41	3–6
		SCAN	2.59	4.30	3.28	0.42	4.39	1.40	5.21	4–7
		Expt.[16]	2.54	–	–	–	–	–	–	–
Cl^-	1.81 Å	PBE	3.07	2.66	3.70	0.79	4.82	1.18	5.77	3–9
		SCAN	3.10	2.70	3.81	0.86	4.76	1.16	6.58	4–10
		Expt.[20]	3.11	–	–	–	–	–	6.4	–
Br^-	1.96 Å	PBE	3.23	2.45	3.81	0.79	4.87	1.33	5.81	3–8
		SCAN	3.28	2.37	4.23	0.89	5.29	1.09	8.75	3–13
		Expt.[16]	3.32	–	–	–	–	–	–	–

3.2.1. Mg^{2+} and Ca^{2+}: Rigid vs. softened divalent hydration under SCAN

Mg^{2+} and Ca^{2+}, both carrying a +2 charge, generate strong electrostatic fields and thus form tightly bound hydration shells. As shown in Figs. 4(a) and 4(b), the ion-oxygen RDF $g_{\text{ION–O}}(r)$ reveals pronounced first peaks (with $g^{\max1}_{\text{Mg–O}} \sim 15$ and $g^{\max1}_{\text{Ca–O}} \sim 10$) and vanishing first minima, indicating highly structured hydration shells (see Table 3 for numerical values).

For Mg^{2+}, the hydration shell remains largely unaffected by the structural disorder introduced by SCAN, as evident in Figs. 4(a), 4(c) and 4(e). The weakening of H-bond network under SCAN enhances the relative strength of ion–water interactions, causing a slight contraction of the first peak position (from 2.09 Å to 2.06 Å) and a sharper first peak ($g^{\max1}_{\text{Mg–O}}$ increases from 13.61 to 14.81), as shown in Table 3. However, the coordination number remains unchanged at 6, and the interstitial region between the first and second shells remains unoccupied ($g^{\mathrm{min1}}_{\mathrm{Mg-O}} \approx 0$). Both PBE and SCAN predict a stable octahedral hydration geometry, consistent with previous theoretical and experimental studies.[57,58] The O–Mg–O angle distribution shows two distinct peaks at 90° and 170°, characteristic of an octahedron, and these remain essentially unchanged under both functionals (Fig. 4(e)). Owing to SCAN's inclusion of intermediate-range van der Waals interactions, the second hydration shell shifts slightly inward (from 4.26 Å to 4.21 Å), further compacting the solvation environment (Fig. 4(a)).

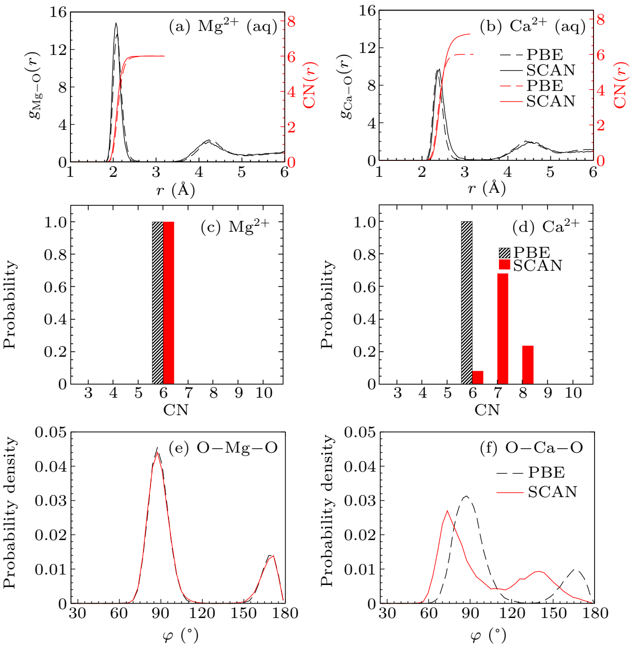

Fig. 4. Hydration structures of Mg^{2+} and Ca^{2+} from PBE and SCAN simulations. (a) and (b) Ion–oxygen RDFs $g_{\mathrm{ION-O}}(r)$ and corresponding running coordination numbers CN(r) for Mg^{2+} and Ca^{2+} aqueous solutions. (c) and (d) Probability distributions of CNs for Mg^{2+} and Ca^{2+}, obtained by integrating the RDFs up to their first minima r^{min1}. (e) and (f) O–ion–O angle distribution functions φ (degree) within the first hydration shell of Mg^{2+} and Ca^{2+}. Solid and dashed lines represent the results from SCAN and PBE, respectively.

In contrast, Ca^{2+} — despite having the same charge — exhibits a more diffuse hydration shell due to its larger ionic radius. This weaker ion–water interaction renders the hydration structure more susceptible to changes in solvent properties. Under SCAN, the first peak shifts outwards from 2.37 Å to 2.41 Å (Fig. 4(b), Table 3), which is in excellent agreement with the x-ray diffraction measurement of 2.42 Å.[15] This outward shift, unlike the slight contraction observed for Mg^{2+}, is accompanied by an increase in coordination number from 6 to 7.16. Part of the second-shell water molecules migrate into the interstitial region ($g^{\mathrm{min1}}_{\mathrm{Ca-O}}$ rises from 0.00 to 0.06), increasing the occupation of the first shell. Simultaneously, the second hydration shell expands (r^{max2} increases from 4.42 Å to 4.55 Å) and becomes less structured, with $g^{\mathrm{max2}}_{\mathrm{Ca-O}}$ decreasing from 2.07 Å to 1.88 Å. As shown in Fig. 4(d), the previously stable octahedral geometry (CN = 6) gives way to a broader distribution of polyhedral configurations, with the pentagonal bipyramid (CN = 7) emerging as the dominant motif. This structural transformation is reflected in the O–Ca–O angle distribution (Fig. 4(f)), where the peak near 90° broadens and shifts to smaller angles, while the shoulder near 165° becomes less pronounced.

3.2.2. Li$^+$, Na$^+$, and K$^+$: Ion-size–dependent hydration restructuring under SCAN

The hydration structures of Li$^+$, Na$^+$ and K$^+$ — monovalent cations with increasing ionic radius — exhibit progressively weaker ion–water electrostatic interactions and increasingly diffuse solvation shells, as reflected in the ion-oxygen RDF ($g_{\mathrm{ION-O}}(r)$, Figs. 5(a)–5(c)). Among them, Li$^+$ maintains the most structured hydration shell, with a pronounced first peak ($g^{\mathrm{max1}}_{\mathrm{Li-O}} \sim 9$) and a vanishing first minimum ($g^{\mathrm{min1}}_{\mathrm{Li-O}} \sim 0$), indicating strong ion–water binding (Fig. 5(a)). This rigidity largely persists under SCAN, despite the softened H-bond network, with only modest structural shifts: r^{max1} contracts from 1.96 Å to 1.93 Å, $g^{\mathrm{max1}}_{\mathrm{Li-O}}$ increases slightly from 8.78 to 8.88, and CN rises marginally from 4 to 4.09 (Table 3). As shown in Fig. 5(d), the originally exclusive tetrahedral coordination (CN = 4) gives way to a broader CN distribution with 3–5 vertices under SCAN, though still dominated by CN = 4 ($\sim$ 90%). As a result, the main peak in the O–Li–O angle distribution at about 105° slightly shifts to a smaller value, and its intensity decreases noticeably (Fig. 5(g)). The intermediate-range vdW interactions among water molecules captured by SCAN bring the second hydration shell of Li$^+$ slightly inward (r^{max2} decreases from 4.07 Å to 4.05 Å).

Na$^+$, with a larger radius and weaker field, shows more pronounced restructuring. SCAN promotes penetration of solvent molecules into the interstitial region and the first hydration shell, increasing CN from 4.81 to 5.43, in agreement with extended x-ray absorption fine-structure spectroscopy (EXAFS) results.[19] The CN distribution broadens from 4–6 to 4–7 vertices, with CN = 6 structures increasing from a minor fraction to 38% and CN = 4 nearly vanishing ($\sim$ 5%) (Fig. 5(e)). The O–Na–O angle distribution correspondingly shifts to smaller angles (Fig. 5(h)), consistent with more compact geometries. Interestingly, r^{max1} remains unchanged at 2.35 Å under SCAN, reflecting a near cancellation between the contraction caused by stronger ion–water attraction and expansion due to increased CN. At the same time, the second shell shifts slightly outward (r^{max2} increases from 4.34 Å to 4.39 Å) and becomes less structured ($g^{\mathrm{max2}}_{\mathrm{Na-O}}$ decreases from 1.46 to 1.30).

Among the three monovalent cations, K$^+$ exhibits the weakest electrostatic interactions with surrounding water molecules due to its largest ionic radius, resulting in the most diffuse and least structured hydration shell. Consequently, SCAN induces the most significant structural reorganization (Figs. 5(c), 5(f) and 5(i), Table 3). The softened H-bond network under SCAN reduces the structuring of the second shell ($g_{\mathrm{K-O}}^{\mathrm{max2}}$ drops from 1.32 to 1.20), while simultaneously increasing the population in the first hydration shell ($g_{\mathrm{K-O}}^{\mathrm{max1}}$ rises from 3.40 to 3.47, with a broader peak). This inward redistribution increases the coordination number from 6.00 to 7.29, accompanied by a slight outward shift in r^{max1} (from 2.70 Å to 2.75 Å), indicating an expanded yet softened solvation shell. As shown in Fig. 5(f), the CN probability distribution reflects this restructuring: under PBE, the hydration geometry spans 4–8 vertices, dominated by CN = 6 polyhedra (39%); under SCAN, the range broadens to 5–10 vertices, with CN = 6 reduced to 23% and CN = 7 (pentagonal bipyramid, triangular prism) becoming the dominant motif (39%). Correspondingly, the O–K–O angle distribution shifts to smaller angles, with the main peak near 80° becoming broader and the satellite peak less discernible, indicative of increased geometric variability and disorder (Fig. 5(i)).

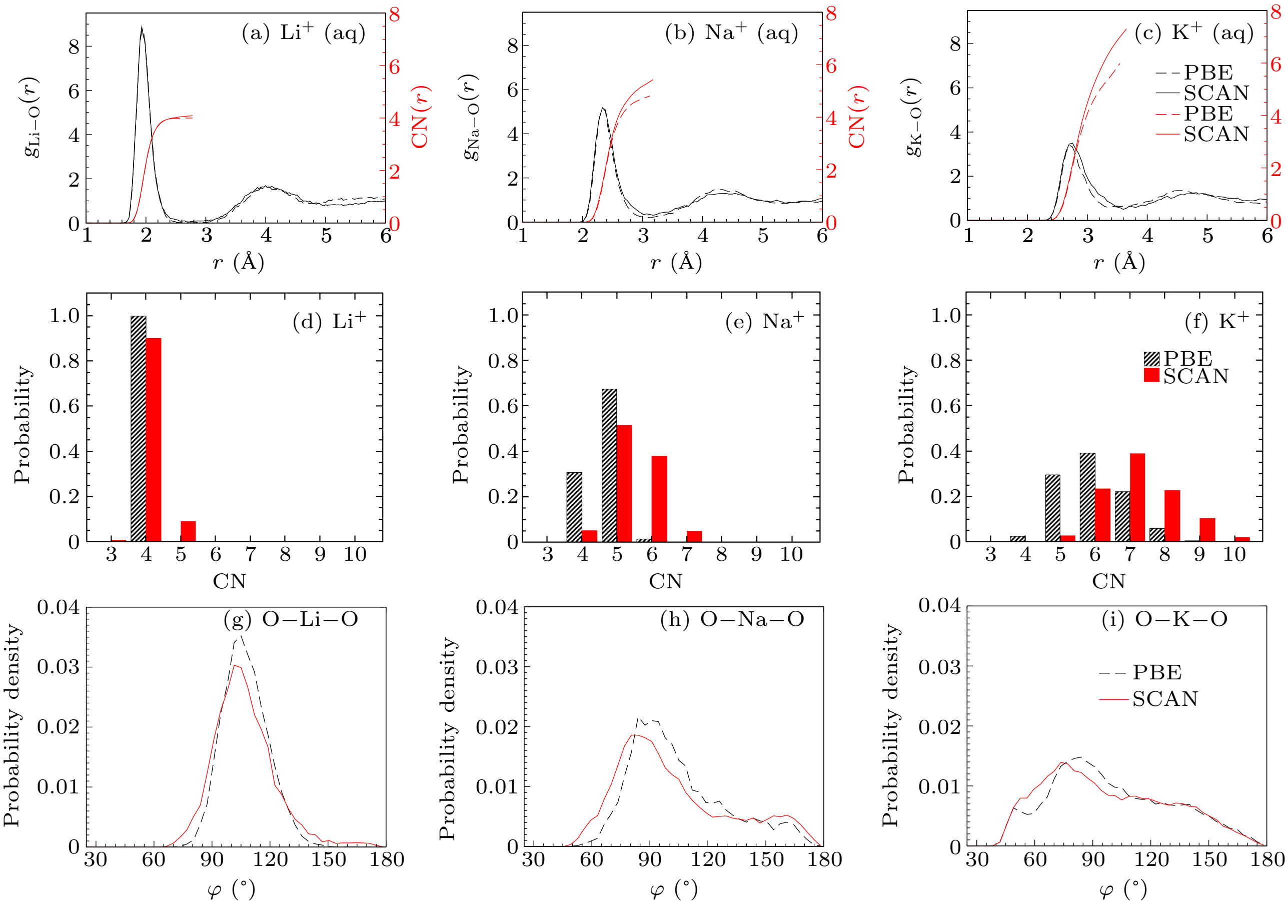

Fig. 5. Hydration structures of monovalent cations from PBE and SCAN simulations. (a)–(c) Ion-oxygen RDFs $g_{\mathrm{ION-O}}(r)$ and corresponding running coordination numbers CN(r) for Li$^+$, Na$^+$, and K$^+$ aqueous solutions. (d)–(f) Probability distributions of CN for Li$^+$, Na$^+$, and K$^+$, obtained by integrating the RDFs up to their first minima r^{min1}. (g)–(i) O–ion–O angle distribution functions φ (degree) within the first hydration shell for the three monovalent cations. Solid and dashed lines represent the results from SCAN and PBE, respectively.

3.2.3. F$^-$, Cl$^-$, Br$^-$: Diffuse anion hydration and SCAN-induced restructuring

The monovalent anions F$^-$, Cl$^-$ and Br$^-$ exhibit increasingly diffuse hydration structures with growing ionic radius, driven by progressively weaker electrostatic interactions with surrounding water molecules. Compared to their cationic counterparts, these anions possess markedly less structured hydration shells, as evidenced by the substantially reduced first-peak intensities in the $g_{\mathrm{ION-O}}(r)$ (Figs. 6(a)–6(c)) and the broader distribution of CN (Figs. 6(d)–6(f), Table 3). As with the cations, this trend reflects the reduced ion–water interaction strength with increasing ionic size. The effect is further enhanced under SCAN, which amplifies structural disorder by softening the hydrogen-bond network, leading to a systematic expansion and delocalization of the hydration shells across all three anions.

Among the three monovalent anions, F$^-$ exhibits the most structured hydration shell, with a pronounced first peak ($g_{\mathrm{F-O}}^{\mathrm{max1}} \sim 4.3$ under PBE) and the deepest first minimum ($g_{\mathrm{F-O}}^{\mathrm{min1}} \sim 0.22$ under PBE), indicative of strong ion–water interactions (Fig. 6(a), Table 3). Despite this rigidity, SCAN softens the hydration structure, as reflected in a broadened and outward-shifted first peak (r^{max1} increases from 2.57 Å to 2.59 Å), as well as a higher first minimum ($g_{\mathrm{F-O}}^{\mathrm{min1}}$ increases to 0.42), which signals increased interstitial occupation. The coordination number rises from 4.41 to 5.21, accompanied by a redistribution of local geometries: tetrahedral configurations (CN = 4) decrease markedly from 59% to 21%, while square pyramids (CN = 5) become dominant, increasing from 38% to 48% (Fig. 6(d)). These changes reflect the weakened H-bond network under SCAN, which facilitates water migration into the first shell and reduces the structural definition of the second shell (r^{max2} increases from 4.37 Å to 4.39 Å; peak intensity decreases from 1.57 to 1.40). The O–F–O angular distribution becomes broader and shifts to smaller angles, indicating increased configurational variability in the solvation structure (Fig. 6(g)).

Although $\mathrm{Cl^-}$ carries the same charge as $\mathrm{F^-}$, its larger ionic radius results in a more diffuse hydration shell, as reflected by the significantly lower first peak and shallower first minimum in $g_{\mathrm{Cl-O}}(r)$ (Fig. 6(b), Table 3). Due to the softening of H-bond network under SCAN, the hydration structure becomes even less structured: the CN increases from 5.77 to 6.58, in excellent agreement with EXAFS measurements of 6.4,[20] and the first shell shifts slightly outward (from 3.07 Å to 3.10 Å), closely matching the experimental value of 3.11 Å.[20] The CN distribution broadens accordingly (Fig. 6(e)): while PBE predicts a solvation structure dominated by square pyramidal (CN = 5, 34%) and octahedral geometries (CN = 6, 33%); SCAN favors higher coordination, with pentagonal pyramids (CN = 7) increasing markedly to 29%, and octahedral geometries remaining prominent (31%). These changes manifest in the O–Cl–O angular distribution (Fig. 6(h)), where peaks near 75° and 90°, associated respectively with CN = 5 and CN = 6 geometries, shift to smaller angles and diminish in intensity. This trend reflects the emergence of more distorted and higher-coordination environments within the first hydration shell under SCAN.

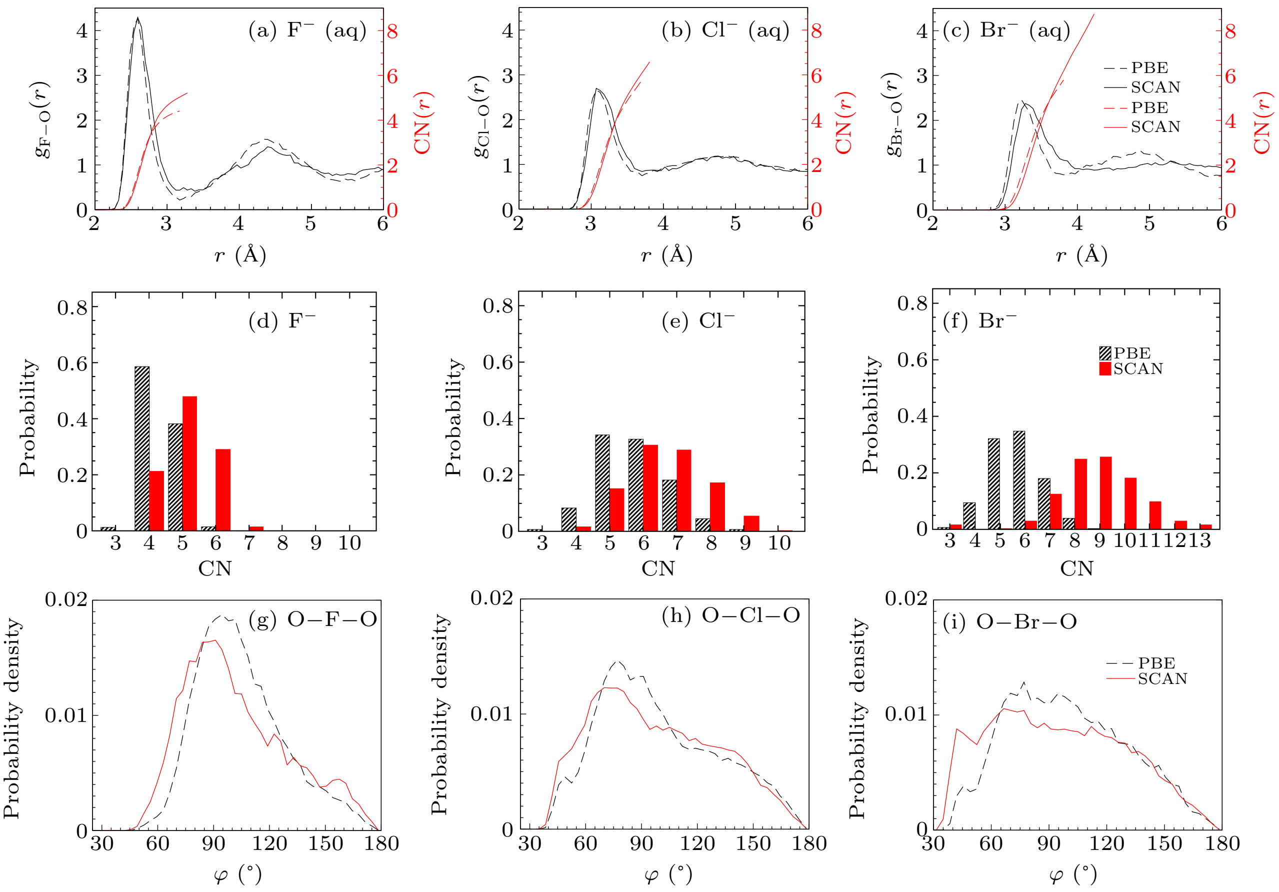

Fig. 6. Hydration structures of monovalent anions from PBE and SCAN simulations. (a)–(c) Ion-oxygen RDFs $g_{\mathrm{ION-O}}(r)$ and corresponding running coordination numbers CN(r) for $\mathrm{F^-}$, $\mathrm{Cl^-}$, and $\mathrm{Br^-}$ aqueous solutions. (d)–(f) Probability distributions of CN for $\mathrm{F^-}$, $\mathrm{Cl^-}$, and $\mathrm{Br^-}$, obtained by integrating the RDFs up to their first minima r^{min1}. (g)–(i) O–ion–O angle distribution functions φ (degree) within the first hydration shell for the three anions. Solid and dashed lines represent results from SCAN and PBE, respectively.

Among the three monovalent anions, $\mathrm{Br^-}$ possesses the largest ionic radius and exhibits the most diffuse hydration shell, on which SCAN imposes the most pronounced structural changes (Fig. 6(c), Table 3). The softening of the H-bond network under SCAN leads to a substantial increase in the first minimum ($g_{\mathrm{Br-O}}^{\mathrm{min1}}$ increases from 0.79 to 0.89), as well as a marked outward shift in its position (r^{min1} increases from 3.81 Å to 4.23 Å). The first peak also shifts outward (r^{max1} increases from 3.23 Å to 3.28 Å) and broadens considerably, consistent with the neutron diffraction value of 3.32 Å.[16] This shell expansion is accompanied by a significant increase in CN, from 5.81 to 8.75. Meanwhile, the CN probability distribution broadens substantially (Fig. 6(f)). Under PBE, the hydration structure spans CN = 3–8 and is dominated by octahedral coordination (CN = 6, 35%). In contrast, SCAN yields a much broader CN distribution ranging from 3 to 13, with octahedral coordination dropping to 3% and nine-coordinate structures emerging as dominant (26%). These rearrangements manifest in the O–Br–O angular distribution (Fig. 6(i)), where characteristic peaks near 95° (octahedron, CN = 6) and 75° (square pyramid, CN = 5) shift to smaller angles and diminish in intensity, while a new satellite peak emerges near 40°, indicative of increasingly distorted hydration environments. Moreover, the second hydration shell becomes highly disrupted: the second peak nearly vanishes, with its intensity $g^{\mathrm{max2}}_{\mathrm{Br-O}}$ dropping from 1.33 to 1.09 — approaching the unstructured baseline value of 1.

While SCAN universally modifies the solvent water structure, its impact on ion hydration is highly ion-specific. For small, high-charge-density cations (Mg^{2+}, Li^{+}; radii > 0.8 Å, see Table 3), both SCAN and PBE predict rigid first-shell geometries, though SCAN produces slightly tighter coordination. For intermediate cations (Ca^{2+}, Na^{+}; 0.8–1.1 Å), SCAN yields higher coordination numbers and broader geometry distributions, whereas PBE favors narrower distributions, exemplified by a predominant octahedral motif for Ca^{2+}. For large, low-charge-density ions (K^{+}, F^{-}, Cl^{-}, Br^{-}; radii > 1.1 Å), SCAN generates more expanded and structurally diverse hydration shells, most notably for Br^{-}, where the second shell is markedly attenuated. These trends highlight SCAN's ability to capture heterogeneous hydration environments, compared with the more rigid descriptions of PBE.

From a theoretical standpoint, SCAN, as a meta-GGA functional representing a higher rung on Jacob's ladder compared with the GGA-level PBE, inherently incorporates intermediate-range van der Waals interactions. Hydration structures arise from a delicate interplay between ion–water and water–water interactions, both of which are influenced by this improved treatment. By weakening the H-bond network, SCAN reshapes the balance between solute–solvent and solvent–solvent interactions, thus replacing the PBE-established equilibrium with a new "SCAN balance" that more sensitively reflects the ion's intrinsic size and charge, leading in certain cases to structural features that are in closer agreement with experimental observations.

A clear example arises for intermediate-size monovalent ions, Na^{+} and Cl^{-}. For both, SCAN predicts first-shell RDF peak positions and coordination numbers in closer agreement with experimental values than PBE. In contrast, improvements are less pronounced for strongly bound small ions (Mg^{2+}, Li^{+}) or very large ions (K^{+}, Br^{-}). We attribute SCAN's advantage for Na^{+} and Cl^{-} to its more balanced treatment of ion–water and water–water interactions: for small ions, hydration is dominated by direct ion–water binding, leaving little scope for functional-dependent corrections, while for large ions, the inherently soft hydration structure remains highly sensitive to functional limitations. In the intermediate regime, however, SCAN's moderation of the hydrogen-bond network yields hydration geometries in notably closer accord with experiment.

3.3. Polarity of water molecules in the hydration shell

We next examine how SCAN alters the polarity of water molecules in the first hydration shell of ions, relative to PBE. Water molecule polarity is closely linked to the strength and topology of the H-bond network. By capturing the intermediate-range van der Waals interactions, SCAN not only adjusts the local geometry and electronic structures of water molecules but also softens the H-bond network, thereby modulating molecular polarization. The electric dipole moment μ of each water molecule is calculated as

$$\mu = R_{\mathrm{H}_1} + R_{\mathrm{H}_2} + 6R_{\mathrm{O}} - 2\sum_{i=1}^{4} R_{w_i}, \tag{1}$$

where R_{H_1}, R_{H_2} and R_{O} are the Cartesian coordinates of the hydrogen and oxygen atoms, and R_{w_i} are the coordinates of the four MLWF centers.

In bulk water, PBE significantly overestimates the H-bond strength and network connectivity, resulting in an average dipole moment μ_{p} = 3.16 D, higher than both the experimental value (2.9 D)[59] and previous theoretical estimate (2.97 D)[34] (Table 4). In contrast, SCAN softens the H-bond network and reduces polarization, yielding $\mu_{\mathrm{s}} = 2.94$ D, in excellent agreement with both.

Table 4. The average dipole moment (in Debye) per water molecule in the first hydration shell of the ionic aqueous solutions considered in this work, as obtained by PBE and SCAN functionals, respectively. The corresponding values for pure water are also shown for comparison.

Functional	Mg^{2+}	Ca^{2+}	Li^{+}	Na^{+}	K^{+}	F^{-}	Cl^{-}	Br^{-}	Pure water
PBE	3.29	3.33	3.10	2.96	2.99	3.17	3.03	3.08	$\mu_{\mathrm{p}} = 3.16$
SCAN	3.23	3.09	2.96	2.78	2.76	3.07	2.85	2.79	$\mu_{\mathrm{s}} = 2.94$

We further evaluate the average dipole moment of water molecules within the first hydration shell of the eight representative ions. As summarized in Table 4, SCAN consistently predicts lower dipole moments than PBE across all cases, indicating a universal tendency to reduce water polarization. These results, in general, also align with the established classification of ions as structure-makers or structure-breakers,[60] reinforcing the interpretation that SCAN captures more realistic ion-induced perturbations in the water network.

For cations, water molecules in the first hydration shells of Mg^{2+} and Ca^{2+} exhibit markedly enhanced dipole moments relative to pure water under both functionals, consistent with their roles as classic structure-makers. For Li^{+}, SCAN predicts a dipole moment slightly higher than that of bulk water, capturing its moderate structure-making character — an effect not captured by PBE. In contrast, K^{+} yields significantly lower dipole moments in both cases, in line with its classification as a structure-breaker. Na^{+}, however, shows lower dipole moments than pure water under both functionals, rendering its borderline assignment less appropriate. For anions, F^{-} exhibits functional-dependent behavior: under PBE, its hydration-shell dipole moment is close to that of pure water, while SCAN predicts a moderate enhancement, deviating from its expected borderline classification. Cl^{-} and Br^{-} show consistently reduced dipole moments under both functionals, reinforcing their roles as structure-breakers. Taken together, SCAN captures the expected polarization trends across different ion categories and offers more nuanced insights into intermediate cases, demonstrating its enhanced handling of both ion–water and water–water interactions.

4. Summary and discussion

We have employed first-principles molecular dynamics simulations based on the SCAN exchange–correlation functional to systematically investigate the structures and electronic properties of eight representative ionic aqueous solutions (Mg^{2+}, Ca^{2+}, Li^{+}, Na^{+}, K^{+}, F^{-}, Cl^{-}, Br^{-}). Compared with the semilocal PBE functional, SCAN yields a more realistic description of solvent water by modifying both the geometry and electronic structure of water molecules, thereby reducing their H-bond propensity. The inclusion of intermediate-range van der Waals interactions softens the H-bond network and brings key structural descriptors into better agreement with experiment.

While SCAN induces a universal reduction in water molecule polarity across all hydration shells, its structural effects on ion solvation are ion-specific. Such effects depend primarily on the strength of ion–water electrostatic interactions, which are governed by ionic charge and size. Divalent cations (Mg^{2+}, Ca^{2+}) maintain highly structured hydration shells; monovalent cations (Li^{+}, Na^{+}, K^{+}) exhibit progressively more diffuse solvation; and monovalent anions (F^{-}, Cl^{-}, Br^{-}) show the most disordered hydration environments. For ions of the same valence, those with larger radii exhibit weaker ion–water interactions and undergo more pronounced structural changes under SCAN, including outward shifts and broadening of hydration shells. SCAN reproduces experimental hydration structures particularly well for intermediate-size monovalent ions (Na^{+}, Cl^{-}). Here, its moderation of the hydrogen-bond network strikes the right balance between ion–water and water–water interactions, yielding hydration geometries consistent with the ions' intrinsic size and charge. Taken together, these results highlight the ability of SCAN to capture both the universal softening of the water network and the ion-specific reorganization of hydration structures. This work provides a reliable first-principles framework for probing ionic solvation and offers mechanistic insight into aqueous systems relevant to chemical, biological, and energy-related processes.

Multi-ion effects, such as ion pairing and collective interactions, may become important at higher concentrations. For the dilute solutions considered here, single-ion hydration provides a sufficient description of the local environment, enabling a clear comparison between SCAN and PBE. Extending to multi-ion systems could be pursued in future work using machine-learning potentials[61] trained on first-principles data, allowing access to larger systems and longer timescales.

Acknowledgments

This project was supported by the National Natural Science Foundation of China (Grant Nos. 12535001, 11935002, and 11525520) and the National Key Research and Development Program of China (Grant No. 2021YFA1400500).

We are grateful for computational resources provided by Hefei advanced computing center, supercomputer TianHe-1A in Tianjin and the High Performance Computing Platform of Peking University, China.

References

[1] Cohen-Tanugi D and Grossman J C 2012 *Nano Lett.* **12** 3602
[2] Sipilä M, Sarnela N, Jokinen T, *et al.* 2016 *Nature* **537** 532
[3] Klimeš J, Bowler D R and Michaelides A 2013 *J. Chem. Phys.* **139** 234702
[4] Gouaux E and Mackinnon R 2005 *Science* **310** 1461
[5] Payandeh J, Scheuer T, Zheng N and Catterall W A 2011 *Nature* **475** 353
[6] Smirnov P R and Trostin V N 2007 *Russ. J. Gen. Chem.* **77** 844
[7] Smirnov P R and Trostin V N 2009 *Russ. J. Gen. Chem.* **79** 1600
[8] Smirnov P R and Trostin V N 2007 *Russ. J. Gen. Chem.* **77** 2101
[9] Swartz C W and Wu X 2013 *Phys. Rev. Lett.* **111** 087801
[10] Tang F, Xu J, Qiu D Y and Wu X 2021 *Phys. Rev. B* **104** 035117
[11] Probst M M, Radnai T, Heinzinger K, Bopp P and Rode B M 1985 *J. Phys. Chem.* **89** 753
[12] Mähler J and Persson I 2012 *Inorg. Chem.* **51** 425
[13] Martinek T, Duboué-Dijon E, Timr Š, *et al.* 2018 *J. Chem. Phys.* **148** 222813
[14] Gillan M J, Alfè D and Michaelides A 2016 *J. Chem. Phys.* **144** 130901
[15] Licheri G, Piccaluga G and Pinna G 1976 *J. Chem. Phys.* **64** 2437
[16] Soper A K and Weckström K 2006 *Biophys. Chem.* **124** 180
[17] Skipper N T and Neilson G W 1989 *J. Phys.: Condens. Matter* **1** 4141
[18] Mason P E, Ansell S and Neilson G W 2006 *J. Phys.: Condens. Matter* **18** 8437
[19] Galib M, Baer M D, Skinner L B, *et al.* 2017 *J. Chem. Phys.* **146** 084504
[20] Dang L X, Schenter G K, Glezakou V A and Fulton J L 2006 *J. Phys. Chem. B* **110** 23644
[21] Kulik H J, Marzari N, Correa A A, *et al.* 2010 *J. Phys. Chem. B* **114** 9594
[22] Näslund L Å, Edwards D C, Wernet P, *et al.* 2005 *J. Phys. Chem. A* **109** 5995
[23] Bian H, Wen X, Li J, *et al.* 2011 *Proc. Natl. Acad. Sci. USA* **108** 4737

[24] Bian H, Li J, Zhang Q, *et al.* 2012 *J. Phys. Chem. B* **116** 14426
[25] Peng J, Cao D, He Z, *et al.* 2018 *Nature* **557** 701
[26] Tian Y, Huang B, Song Y, *et al.* 2024 *Nat. Commun.* **15** 7834
[27] Tian Y, Song Y, Xia Y, *et al.* 2024 *Nat. Nanotechnol.* **19** 479
[28] Car R and Parrinello M 1985 *Phys. Rev. Lett.* **55** 2471
[29] Kresse G and Hafner J 1993 *Phys. Rev. B* **47** 558
[30] Distasio Jr R A, Santra B, Li Z, Wu X and Car R 2014 *J. Chem. Phys.* **141** 084502
[31] Zhou L, Xu J, Xu L and Wu X 2019 *J. Chem. Phys.* **150** 124505
[32] Sun J, Ruzsinszky A and Perdew J P 2015 *Phys. Rev. Lett.* **115** 036402
[33] Sun J, Remsing R C, Zhang Y, *et al.* 2016 *Nat. Chem.* **8** 831
[34] Chen M, Ko H Y, Remsing R C, *et al.* 2017 *Proc. Natl. Acad. Sci. USA* **114** 10846
[35] Giannozzi P, Andreussi O, Brumme T, *et al.* 2017 *J. Phys.: Condens. Matter* **29** 465901
[36] Giannozzi P, Baroni S, Bonini N, *et al.* 2009 *J. Phys.: Condens. Matter* **21** 395502
[37] Bankura A, Santra B, Distasio Jr R A, *et al.* 2015 *Mol. Phys.* **113** 2842
[38] Pham T A, Ogitsu T, Lau E Y and Schwegler E 2016 *J. Chem. Phys.* **145** 154501
[39] Xu J, Sun Z, Zhang C, *et al.* 2021 *Phys. Rev. Mater.* **5** L012801
[40] Hamann D R, Schlüter M and Chiang C 1979 *Phys. Rev. Lett.* **43** 1494
[41] Vanderbilt D 1985 *Phys. Rev. B* **32** 8412
[42] Hamann D R 2013 *Phys. Rev. B* **88** 085117
[43] Schlipf M and Gygi F 2015 *Comput. Phys. Commun.* **196** 36
[44] Nosé S 1984 *J. Chem. Phys.* **81** 511
[45] Hoover W G 1985 *Phys. Rev. A* **31** 1695
[46] Sun Z, Zheng L, Chen M, *et al.* 2018 *Phys. Rev. Lett.* **121** 137401
[47] Bankura A, Vincenzo C and Klein M L 2014 *Mol. Phys.* **112** 1448
[48] Payne M C, Teter M P, Allan D C, Arias T A and Joannopoulos J D 1992 *Rev. Mod. Phys.* **64** 1045
[49] Grossman J C, Schwegler E, Draeger E W, Gygi F and Galli G 2004 *J. Chem. Phys.* **120** 300
[50] Schwegler E, Grossman J C, Gygi F and Galli G 2004 *J. Chem. Phys.* **121** 5400
[51] Gaiduk A P, Zhang C, Gygi F and Galli G 2014 *Chem. Phys. Lett.* **604** 89
[52] Soper A K and Benmore C J 2008 *Phys. Rev. Lett.* **101** 065502
[53] Marzari N and Vanderbilt D 1997 *Phys. Rev. B* **56** 12847
[54] Silvestrelli P L, Marzari N, Vanderbilt D and Parrinello M 1998 *Solid State Commun.* **107** 7
[55] Luzar A and Chandler D 1996 *Phys. Rev. Lett.* **76** 928
[56] Tang F, Shi K and Wu X 2023 *J. Chem. Phys.* **159** 164502
[57] Lightstone F C, Schwegler E, Hood R Q, Gygi F and Galli G 2001 *Chem. Phys. Lett.* **343** 549
[58] Marcus Y 1983 *J. Solution Chem.* **12** 271
[59] Badyal Y S, Saboungi M L, Price D L, *et al.* 2000 *J. Chem. Phys.* **112** 9206
[60] Marcus Y 2009 *Chem. Rev.* **109** 1346
[61] Zhang L, Han J, Wang H, Car R and E W 2018 *Phys. Rev. Lett.* **120** 143001
[62] Vinogradov E V, Smirnov P R and Trostin V N 2003 *Russ. Chem. Bull.* **52** 1253
[63] Glezakou V A, Chen Y, Fulton J L, Schenter G K and Dang L X 2006 *Theor. Chem. Acc.* **115** 86